catalysts

MDPI

Article

Improved Photoelectrochemical Performance of $BiVO_4$ for Water Oxidation Enabled by the Integration of the Ni@NiO Core–Shell Structure

Jun-Yuan Cui [1,†], Shi-Shi Zhu [1,†], Yang Zou [1], Yan Zhang [1], Shao-Yu Yuan [1], Tian-Tian Li [1], Shi-Yi Guo [1,*], Hong Liu [1,2,*] and Jian-Jun Wang [1,3,*]

1 State Key Laboratory of Crystal Material, Shandong University, Jinan 250100, China
2 Institute for Advanced Interdisciplinary Research (IAIR), University of Jinan, Jinan 250022, China
3 Shenzhen Research Institute of Shandong University, Shandong University, Shenzhen 518057, China
* Correspondence: syguo@sdu.edu.cn (S.-Y.G.); hongliu@sdu.edu.cn (H.L.); wangjianjun@sdu.edu.cn (J.-J.W.)
† These authors contributed equally to this work.

Abstract: The development of highly efficient and stable photoelectrode materials is of significant importance for the conversion of solar energy into chemical fuels. Herein, a novel Ni@NiO/$BiVO_4$ photoanode is designed and prepared for efficient water splitting by the deposition of Ni particles on the surface of $BiVO_4$ with subsequent thermal treatment. The integration of the Ni@NiO core–shell structure can efficiently passivate the surface states and accelerate the oxygen evolution kinetics along with the in situ-generated NiOOH, consequently contributing to the significantly improved charge separation efficiency. The resulting Ni@NiO/$BiVO_4$ photoelectrode enabled a photocurrent density of 2.6 mA/cm^2 with a surface charge separation efficiency of nearly 80% at the potential of 1.23 V_{RHE}—much better than the unmodified $BiVO_4$ (1.8 mA/cm^2, 64%).

Keywords: $BiVO_4$; Ni@NiO; photoelectrochemical; water oxidation

check for updates

Citation: Cui, J.-Y.; Zhu, S.-S.; Zou, Y.; Zhang, Y.; Yuan, S.-Y.; Li, T.-T.; Guo, S.-Y.; Liu, H.; Wang, J.-J. Improved Photoelectrochemical Performance of $BiVO_4$ for Water Oxidation Enabled by the Integration of the Ni@NiO Core–Shell Structure. *Catalysts* **2022**, *12*, 1456. https://doi.org/10.3390/catal12111456

Academic Editor: Jae Sung Lee

Received: 6 October 2022
Accepted: 14 November 2022
Published: 17 November 2022

1. Introduction

In order to address the global energy crisis and environmental problems caused by the excessive use of fossil fuels, a number of researchers have been engaged with the energy conversion of solar energy to chemical fuels through photoelectrochemical cells [1]. In recent decades, metal oxide semiconductors have attracted considerable attention as photoelectrode materials due to their favorable valence band positions for water oxidation reactions and have been extensively studied [2], including TiO_2, Fe_2O_3, WO_3 and $BiVO_4$ [3]. Among them, monoclinic scheelite-phase $BiVO_4$ has emerged as a promising photoanode for water oxidation as a result of its narrow bandgap and appropriate band edge positions [4]. However, the photoelectrochemical performance of $BiVO_4$ is still far from the theoretical value (7.5 mA cm^{-2}) [5] ascribed to the severe charge recombination, slow oxygen evolution reaction kinetics and poor stability.

Up to the present time, plenty of strategies have been used to optimize the efficiency of $BiVO_4$ for water splitting. In particular, transition metal-based promoters have been explored to promote the reaction kinetics on the surface due to their high-efficiency OER activity. For instance, $FeCoO_x$ has been demonstrated as a co-catalyst on the surface of a planar BVO_4 photoanode to effectively reduce the water oxidation barrier between the photoanode and the electrolyte [6]. Similarly, metal–organic frameworks on the surface of $BiVO_4$ can provide active sites for OER to improve the water oxidation capacity of the resulting photoanode [7,8]. Additionally, a thin layer of in situ-formed FeNi oxyhydroxide on $BiVO_4$ can effectively prevent the precipitation of V^{5+} through the formation of the V-O-Ni bond at the interface, thereby improving the photoelectrochemical stability of the resultant $BiVO_4$ photoanode [4]. However, the electron–hole recombination centers

at the interface of the heterostructures may be introduced and detrimentally affect the performance of $BiVO_4$ [9].

Promisingly, inserting an electron mediator, such as Au [10], Pt [11], Ni [12], etc., in the middle of the heterojunctions can effectively improve the bulk charge separation. Among them, Ni and its oxides are attractive materials both as passivation layers and oxygen evolution catalysts, and have been widely studied for photoelectrochemical energy conversion [13,14]. Impressively, Lee et al. constructed a metal–insulator–semiconductor structure of NiO_x/Ni/n-Si for efficient water splitting [15]. The nickel islands with a high-work function act as nano-emitters to efficiently collect the charges in the metal–insulator–semiconductor (MIS) structure, with NiO_x expanding the Schottky barrier [16]. Furthermore, Malara et al. found that NiO_x could be further oxidized to form high-valent Ni oxides during alkaline OER, contributing to the improved photoelectrochemical process [17]. Inspired by this, we propose a new strategy to improve the performance of $BiVO_4$ for photoelectrochemical water splitting. A layer of Ni particles can be deposited on the surface of $BiVO_4$ and then a thin NiO layer is in situ formed simply by heat treatment. The formed Ni@NiO core–shell structure can be used as a highly active OER co-catalyst and can passivate the surface states of $BiVO_4$ to improve the efficiency for water oxidation.

2. Results and Discussion

As shown in Figure 1a, the $BiVO_4$ electrode was prepared according to a previously reported method [18], and the Ni@NiO/$BiVO_4$ photoanode was obtained by spin-coating Ni nanoparticles that were prepared by a solution method on the surface of $BiVO_4$ followed by annealing in air. The $BiVO_4$ and Ni@NiO/$BiVO_4$ electrodes both show a porous structure composed of worm-like nanoparticles (Figure 1b,c), consistent with the literature [19]. Compared with the bare $BiVO_4$, more fine nanoparticles appeared on the surface of the Ni@NiO/$BiVO_4$ photoanode. However, no additional diffraction peaks were observed (Figure S1) in the X-ray diffraction (XRD) spectra, except for the peaks assigned to the monoclinic phase of pristine $BiVO_4$ (No. 14-0688)—probably due to the low content and small future size [4]. To figure out the phase composition of Ni species, X-ray diffraction (XRD) was conducted directly on the freshly prepared Ni nanoparticles as well as the particles after annealing at 400 °C. The results reveal that Ni nanoparticles display a characteristic peak at 44.5° corresponding to the (111) crystal facet of cubic Ni (No.04-0850, Figure S2). Additionally, several weak characteristic peaks were observed at 37.2°, 43.2° and 62.8°, indexed to the (101), (012) and (110) crystal facet of hexagonal NiO (No.44-1159) after annealing, thus, proving the formation of the Ni@NiO core–shell structure [20]; the peaks assigned to Ni were significantly intensified due to the improved crystallinity and the grown particle size caused by agglomeration during the annealing process.

Furthermore, the TEM and high-resolution TEM (HRTEM) characterization on $BiVO_4$ and Ni@NiO/$BiVO_4$ were conducted, and the results are shown in Figures S3 and 1d. Clearly, some core–shell nanoparticles were observed on the surface of $BiVO_4$, consistent with the observation of SEM. In addition, the heterostructure formed between the core–shell structure and $BiVO_4$ was confirmed with the three observed areas assigned to $BiVO_4$, Ni and NiO, respectively, along with the results of XRD, SEM and XPS [21–23]. Specifically, the observed d-spacing of 0.461 nm corresponds to the (011) crystal plane of $BiVO_4$, the d-spacing of 0.203 nm on the inner particles of the core–shell structure can be assigned to the (111) plane of the Ni nanoparticles, and the d-spacing of 0.205 nm on the shell of the core–shell structure corresponds to the (012) crystal plane of NiO, which are also consistent with the XRD results.

XPS was conducted to further prove the heterojunction formed by the core–shell structure and $BiVO_4$ and study the chemical states of the elements. In the high-resolution XPS spectrum of the Bi element (Figure 2a), the peak binding energies around 158.74 and 164.04 eV could be assigned to Bi $4f_{7/2}$ and Bi $4f_{5/2}$ of Bi^{3+} in the pure $BiVO_4$ photoanode [24]. Furthermore, the V^{5+} in the products was disclosed by the V 2p peak centers at around 516.40 and 523.80 eV (Figure 2c) in the $BiVO_4$ photoanode [25]. In the fine spectrum

of Ni 2p, the Ni $2p_{3/2}$ peaks centered at ~856 eV and ~852 eV were attributed to Ni^{2+} and Ni^0, respectively, which proved the existence of the Ni/NiO core–shell structure [26–29]. Only a trace of Ni^0 species was found in the 2p peak of Ni as a result of the detection depth of XPS—which is relatively shallow—and the presence of the annealed oxide layer (Figure S3d) [30]. Compared with pure $BiVO_4$, the positions of Bi 4f, O 1s, and V 2p exhibit a positive shift after being surface-loaded with a Ni@NiO core–shell structure, indicating that the electron density of $BiVO_4$ decreases, which can be ascribed to the surface binding interaction between the $BiVO_4$ and Ni@NiO core–shell structures, thus, inducing the electron transfer from $BiVO_4$ to Ni@NiO core–shell structures [31]. For instance, the Bi $4f_{7/2}$ peak of Ni@NiO/$BiVO_4$ was shifted by 0.37 eV toward the higher-binding energy, which is close to that of the treated $BiVO_4$ with HCl [25], suggesting a stronger interaction between $BiVO_4$ and Ni@NiO with the formation of heterojunction [23].

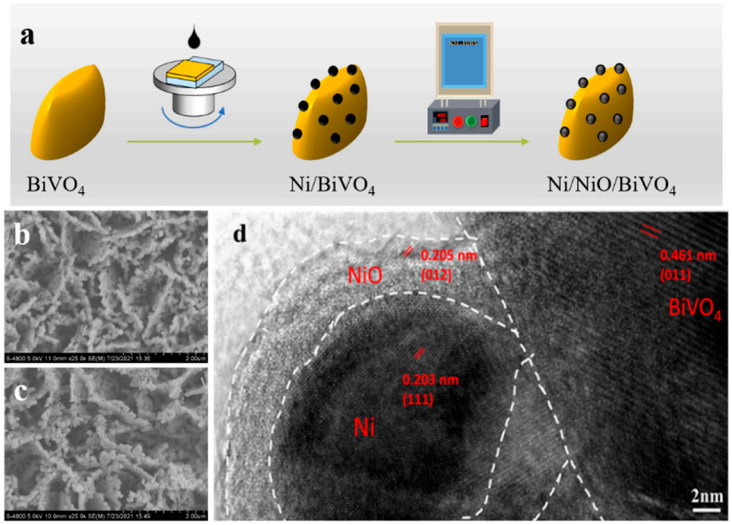

Figure 1. (**a**) The synthetic process of the heterostructure photoanode. SEM images of (**b**) bare $BiVO_4$ and (**c**) Ni@NiO/$BiVO_4$.; (**d**) a HRTEM image of the Ni@NiO/$BiVO_4$ photoanode.

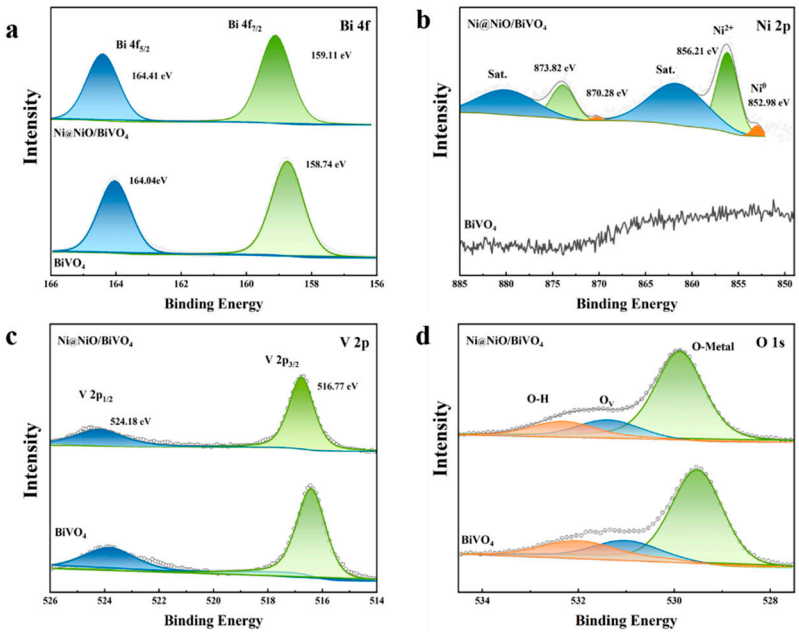

Figure 2. XPS of $BiVO_4$ and Ni@NiO/$BiVO_4$ photoanodes. (**a**) Bi 4f; (**b**) Ni 2p; (**c**) V 2p; and (**d**) O 1s.

The optical properties of $BiVO_4$ and Ni@NiO/$BiVO_4$ films were measured by UV–vis–NIR absorption spectroscopy. In the UV–vis–NIR spectra, both the absorption edges of the obtained photoanodes are located at approximately 500 nm; an increase in the optical absorption intensity of Ni@NiO/$BiVO_4$ films can be clearly observed over 500 nm, which may be attributed to the surface plasmon resonance effect of metallic Ni nanoparticles [32].

The photoelectrochemical performance of the prepared $BiVO_4$ and Ni@NiO/$BiVO_4$ electrodes was evaluated in a typical three-electrode cell (Figure 3b–f). Generally, the spin-coating cycle and annealing temperature show critical effect on the PEC performance (Figure S4) due to their modulation of the coverage, crystallinity and agglomeration of Ni@NiO on $BiVO_4$. As displayed in Figure 3b, the optimized Ni@NiO/$BiVO_4$ photoelectrode exhibits a significantly improved photocurrent in contrast to the bare $BiVO_4$, where a photocurrent of 2.6 mA/cm^2 at 1.23 V_{RHE} is obtained, much higher than that of $BiVO_4$ (1.8 mA/cm^2). No significant change in onset potential was observed, this was likely due to the V^{4+}/V^{5+} redox peak near the onset potential [33]. Assuming that the Faraday efficiency is 100%, the applied bias photocurrent efficiency (ABPE) of $BiVO_4$ and Ni@NiO/$BiVO_4$ photoanodes was calculated from the LSV curve to evaluate the solar energy conversion efficiency in the PEC process for water splitting (Figure 3c). The maximum ABPE of the bare $BiVO_4$ photoanode is 0.48% at 0.80 V, while the maximum ABPE of the Ni@NiO/$BiVO_4$ photoanode is largely enhanced to about 0.73% at 0.77 V vs. RHE, suggesting significant efficiency improvement for solar water splitting compared with the $BiVO_4$ photoanode (Table S1). The PEC stability of $BiVO_4$ and Ni@NiO/$BiVO_4$ were studied at 1.23 V_{RHE} with/without chopping illumination (Figure 3d,e). Both electrodes show good optical switching characteristics and a fast response, and apparently the Ni@NiO/$BiVO_4$ photoanodes exhibited slightly enhanced stability compared with the bare $BiVO_4$ [34]. After the operation for 60 min, the photocurrent of the heterostructure photoanode is still 2.2 times that of $BiVO_4$ with the maintained percentage of the initial current enhanced from 49.31% to 62.64%, implying the superiority of the heterojunction structure. Clearly, the surface charge separation efficiency of Ni@NiO/$BiVO_4$ is significantly higher than that of the bare $BiVO_4$ photoanodes (Figure 3f), suggesting that the formation of the Ni@NiO core–shell structure on the surface can accelerate surface charge transfer, promote water oxidation kinetics and contribute to the improved PEC performance [35].

In order to understand the work mechanism of the heterostructure photoanode well, the catalytic chemistry on the surface and the transportation and separation of the photo-generated charge carriers were investigated. When the electrochemical OER activity without illumination was evaluated within a wider potential range (Figure 4a), the Ni@NiO/$BiVO_4$ photoanode exhibited a lower overpotential and higher water oxidation current than the bare $BiVO_4$ photoanode, suggesting the higher OER activity on the surface of Ni@NiO/$BiVO_4$. Furthermore, the charge-transfer rate at the photoanode/electrolyte interface is related to the electrochemically active surface area (ECSA), and a low ECSA may result in the accumulation of photo-generated holes that reach the surface, detrimentally promoting their recombination with the photo-generated electrons [36–38]. As shown in Figure 4b, the relationship between the capacitive currents and the scanning rates of the two photoanodes was calculated from their cyclic voltammogram (Figure S5), where the slope is proportional to the ECSA of the photoanode. Interestingly, the ECSA of the Ni@NiO/$BiVO_4$ photoanode is 36% higher than that of the pure $BiVO_4$, indicating that the integration of Ni@NiO core–shells brings more active sites [39] for the oxygen evolution reaction and simultaneously implies that the enhanced intrinsic catalytic activity of the modified $BiVO_4$ is also an important factor for the enhanced performance. To further verify the critical role of the surface Ni@NiO core–shell in enhancing the photoelectrochemical performance of $BiVO_4$, the behavior of the photo-generated charge carrier was studied by the open circuit photovoltage (OCP, Figures 4c and S6). The degree of band bending is determined by the built-in potential, minority carrier accumulation, and charge recombination in the photoanode/electrolyte junction. Generally, larger band bending at the photoanode/electrolyte interface is more favorable for the photo-generated electron–hole separation. Basically, a

more positive OCV value in the dark and a more negative OCV_{light} under illumination imply larger band bending [40]. Compared with bare $BiVO_4$, the energy band bending of Ni@NiO/$BiVO_4$ is significantly improved with a more positive OCV_{dark}, indicating that the Ni@NiO core–shell can effectively passivate the surface states of $BiVO_4$ [41]. The lifetime decay process of the photo-generated charge carrier when the light is turned off can also be used to study the properties of the semiconductor/electrolyte interface. The accumulation of charge carriers due to band bending enables a rapid recombination of photo-generated electrons and holes in the dark [42]. Clearly, the photoanode of Ni@NiO/$BiVO_4$ exhibits a faster decay (Figure 4d), indicating the rapid separation of photo-generated electrons and holes at the semiconductor/electrolyte interface under illumination.

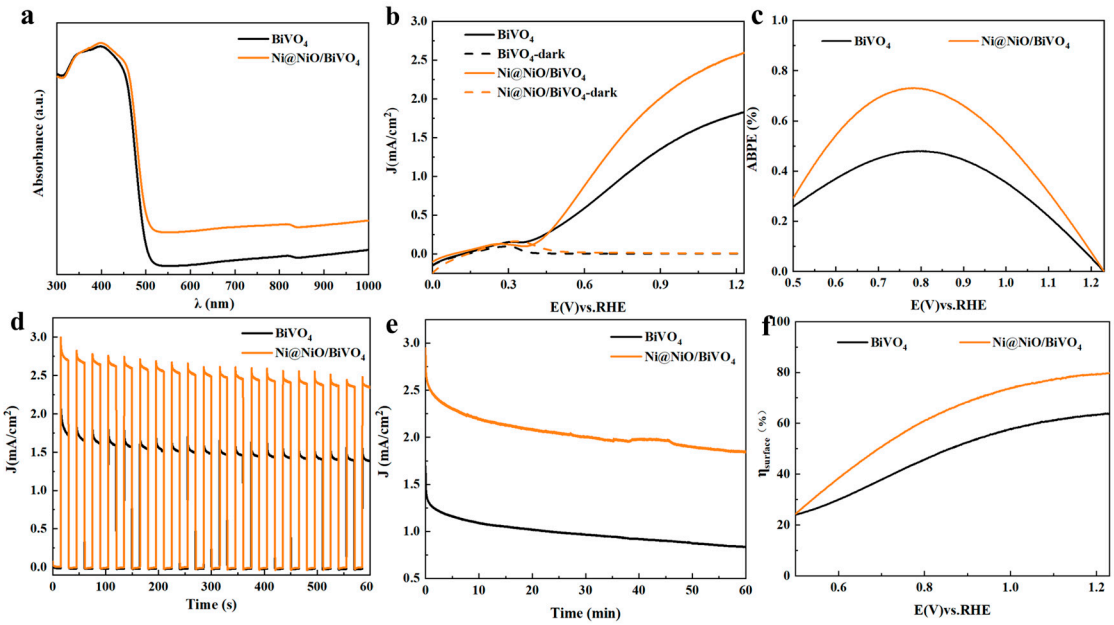

Figure 3. (**a**) Absorption spectra of $BiVO_4$ and Ni@NiO/$BiVO_4$ films. (**b**) LSV curves of $BiVO_4$ and Ni@NiO/$BiVO_4$ photoanodes; (**c**) ABPE and (**d**) J-t curves measured at 1.23 V_{RHE} under chopped AM 1.5G illumination in a borate buffer solution; (**e**) long-term J-t curves of $BiVO_4$ and Ni@NiO/$BiVO_4$ photoanodes; (**f**) surface charge separation efficiency.

To further study the charge-transfer process, EIS measurements were carried out (Figure 4e) and the results were fitted using the corresponding equivalent circuit in the inset. The model consists of R_s and two RC circuits connected in series. R_s refers to the ohmic resistance generated by the electrolyte, electrical contacts and wires; R_{tr} represents the bulk resistance; and R_{ct} corresponds to the charge-transfer resistance at the photoelectrode/electrolyte interface with CPE representing the ideal capacitor for the corresponding process [43]. Compared with the bare $BiVO_4$ (744.6 Ω), R_{tr} of the Ni@NiO/$BiVO_4$ sample was reduced to 519.7 Ω. It was deduced that the decrease in R_{tr} was due to the close contact between the Ni@NiO core–shell and $BiVO_4$ through annealing as well as the Schottky junction formed between the Ni@NiO core–shell structure and $BiVO_4$ [12,15]. In addition, the R_{ct} of Ni@NiO/$BiVO_4$ is significantly reduced from 668.6 Ω of bare $BiVO_4$ to 226.5 Ω, indicating that Ni@NiO is a good co-catalyst that can accelerate the slow oxygen evolution kinetics on the $BiVO_4$ surface. This result is also consistent with the result of surface separation efficiency. As shown in Figure 4f, there is a clear intensity difference in the peaks around 493 nm related to the radiative recombination of holes in the O 2p band and electrons in the V 3d band, which is related to the electron–hole recombination in the bulk [44,45]. While for wavelengths greater than 520 nm, $BiVO_4$ does not show intrinsic light absorption, and the emission peaks may be related to the surface states of $BiVO_4$ [46]. Clearly, the Ni@NiO/$BiVO_4$ photoanode exhibited a reduced PL peak in less than 520 nm,

indicating that the deposition of Ni@NiO core–shells can significantly reduce the bulk recombination of photo-generated electron–hole pairs due to the Schottky junction formed between the Ni@NiO core–shell and $BiVO_4$ [12,15]. In addition, Ni@NiO/$BiVO_4$ exhibited a smaller PL intensity in the range greater than 520 nm, which was due to the Ni@NiO core–shell structure effectively passivating the surface states, which further promoted the charge separation; this is also consistent with the above results.

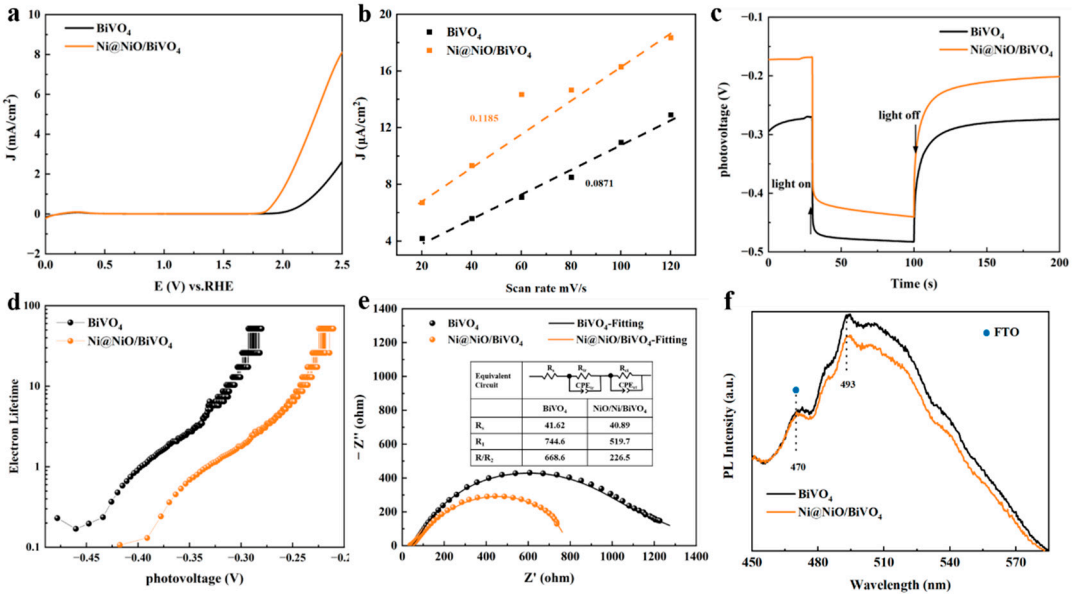

Figure 4. (**a**) LSV curves in the dark. (**b**) Plot of the capacity current as a function of the scan rate. (**c**) Open-circuit voltages of $BiVO_4$, Ni/$BiVO_4$ and Ni@NiO/$BiVO_4$ photoanodes in the dark and under illumination. (**d**) The corresponding lifetimes indicate the OCP decay times of $BiVO_4$, Ni/$BiVO_4$ and Ni@NiO/$BiVO_4$ photoanodes after turning off the light. (**e**) EIS Nyquist plot at an open circuit voltage under illumination. (**f**) Photoluminescence spectroscopy of $BiVO_4$, Ni/$BiVO_4$ and Ni@NiO/$BiVO_4$ photoanodes.

Furthermore, after the PEC operation for 10 mins, the role of the Ni@NiO core–shell becomes more obvious (Figure S7a–c). To explore the reason for this change, we performed XPS measurements on the samples. It was found that the Ni^{3+} peak appeared in the spectrum of Ni@NiO/$BiVO_4$ instead of the Ni^0 peak. This result indicates that the Ni species was oxidized during the PEC process and the Ni core was gradually oxidized to Ni oxides with the in situ formation of NiOOH on the surface, consistent with the previously reported results [15,47]. The generated NiOOH is also an excellent oxygen evolution catalyst and enables the accelerated oxygen evolution kinetics on the surface of the Ni@NiO/$BiVO_4$ photoanode [30], thus, contributing to the improved PEC performance.

Summarily, the integration of the Ni@NiO core shell on the surface of $BiVO_4$ plays an important role in improving the PEC performance (Figure 5). Usually, the poor oxygen evolution kinetics and surface states of $BiVO_4$ result in the serious recombination of the photo-generated holes and electrons on the surface of $BiVO_4$. The introduction of the Ni@NiO core–shell structure on the surface of $BiVO_4$ can form a heterojunction to promote the charge separation in the bulk; the photo-generated holes can be transferred from the valence band of $BiVO_4$ to Ni@NiO for the water oxidation reaction, promoting the charge-transfer process. On the other hand, the Ni@NiO core–shell structure on the surface can not only improve the oxygen evolution kinetics of $BiVO_4$, but also passivate the surface state, thereby significantly improving the charge separation efficiency at the $BiVO_4$/electrolyte interface (Figure 5b) [48]. Additionally, the conversion of the Ni@NiO core–shell into NiOOH during the PEC process enables the acceleration of the photoelectrochemical reaction process.

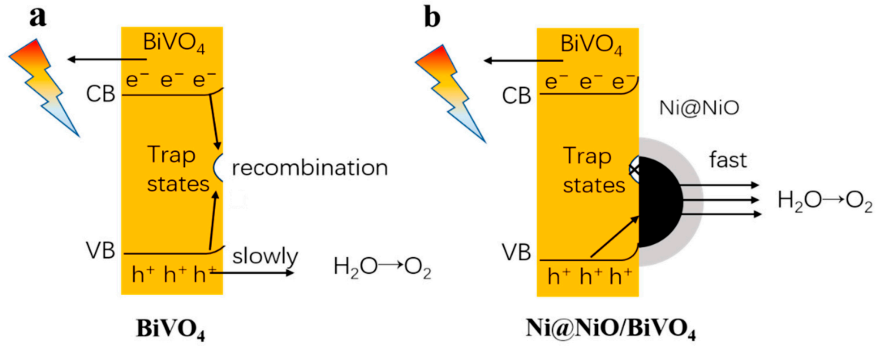

Figure 5. Photoelectrochemical water splitting mechanism of (**a**) $BiVO_4$ and (**b**) Ni@NiO/$BiVO_4$ photoanodes under illumination.

3. Materials and Methods

3.1. Materials

Bismuth nitrate pentahydrate ($Bi(NO_3)_3{\cdot}5H_2O$, 99.0%), *p*-benzoquinone (≥98.0%) and vanadyl acetylacetonate ($VO(acac)_2$, 98%) were obtained from Sigma-Aldrich, Co. Ltd. (St. Louise, MO, USA). Potassium iodide (KI, ≥99.0%), dimethyl sulfoxide (DMSO, AR), nickel nitrate hexahydrate ($Ni(NO_3)_2{\cdot}6H_2O$, 98.5%), oleic acid ($C_{18}H_{34}O_2$, AR), sodium borohydride ($NaBH_4$, ≥98.0%) and sodium dodecyl sulfate (SDS, CP) were purchased from Sinopharm Chemical Reagent Co., Ltd. (Shanghai, China).

3.2. Preparation of the Worm-Like $BiVO_4$ Film

The $BiVO_4$ film on FTO was prepared according to a modified method reported by Choi [18]. Typically, the $Bi(NO_3)_3$ solution (0.04 M) was prepared by dissolving $Bi(NO_3)_3{\cdot}5H_2O$ in 50 mL of the KI (0.4 M) solution with the pH adjusted to 1.7 by HNO_3. Afterwards, 20 mL of the *p*-benzoquinone (0.23 M) solution in absolute ethanol was slowly added into the as-prepared $Bi(NO_3)_3$ solution, and then the resultant solution was vigorously stirred for 40 min at room temperature. The precursor of BiOI nanosheets was prepared via electrodeposition in a typical three-electrode cell. FTO (3 × 1 cm^2) serves as the working electrode (WE) with a saturated Ag/AgCl as the reference electrode (RE) and platinum foil (1.5 × 1.5 cm^2) as the counter electrode (CE). Cathodic deposition was conducted potentiostatically at −0.147 V vs. SCE at room temperature for 420 s. The obtained orange BiOI precursor was rinsed with DI water to remove the excess electrolyte on the surface. Next, 0.11 mL of the dimethyl sulfoxide (DMSO) solution containing vanadyl acetylacetonate ($VO(acac)_2$) (0.2 M) was placed on the BiOI film (1 × 2 cm^2), and the film was annealed in a muffle furnace at 450 °C (ramping rate = 2 °C min^{-1}) for 2 h. The $BiVO_4$ film electrode was obtained intact on the FTO with the color changing from orange to yellow after removing the excess V_2O_5 by soaking it in the NaOH solution (1 M) for 30 min with mild stirring.

3.3. Preparation of Ni Nanoparticle

The nickel nanoparticles were synthesized according to a previously reported method with a slight modification [49]. Typically, 3.07 g of SDS, 1.3 mL of OA and 0.31 g of $Ni(NO_3)_2{\cdot}6H_2O$ were sequentially added to 107 mL of DI water whilst stirring vigorously for 30 min to obtain a uniform solution. Afterwards, 0.05 g of $NaBH_4$ was added to the above solution whilst stirring for 1 h to obtain Ni particles.

3.4. Preparation of Ni@NiO/$BiVO_4$ Photoanode

The freshly prepared Ni particles were spin-coated on the freshly prepared $BiVO_4$ film with a rotation speed of 2000 rpm/s and a spin-coated time of 15 s. Repeated different cycles can be applied to obtain different samples of Ni/$BiVO_4$. Finally, the Ni/$BiVO_4$ samples were annealed in a muffle furnace at 400 °C for 1 h.

3.5. Materials Characterization

The X-ray diffraction patterns of all the electrodes were recorded on a Rigaku X-ray diffractometer D/Max-2200/PC (Nishiko Corporation of Japan, Tokyo, Japan) equipped with Cu-Kα radiation (40 kV, 20 mA). The optical properties of all the samples were estimated by a UV–vis–IR spectrophotometer (Cary 5000) (Agilent Technologies, Palo Alto, CA, USA) equipped with an integration sphere unit using a diffuse reflection method. The structure and morphology of all the samples were studied using a JSM6701E field emission scanning electron microscope (JEOL, Tokyo, Japan) and transmission electron microscopy Talos F200x (Thermo Fisher Scientific, Waltham, MA, USA). XPS was recorded on a Thermo Scientific K-Alpha photoelectron spectrometer (Thermo Fisher Scientific). The photoluminescence (PL) spectra were obtained on a F-4500 FL Spectrophotometer (Hitachi, Tokyo, Japan) under a laser excitation of 400 nm.

3.6. Photoelectrochemical Measurements

The PEC performance of all the samples was evaluated by an electrochemical workstation (CHI 660E) in a typical three-electrode cell containing a 0.5 M phosphate-buffered saline (pH = 9). The bare $BiVO_4$ and Ni@NiO/$BiVO_4$ electrodes served as the working electrode; the saturated Ag/AgCl electrode and platinum foil acted as the RE and CE, respectively. A xenon lamp simulating sunlight AM 1.5G (100 mW/cm^2) was used as the light source. The linear sweep voltammetry curves were recorded within a potential range from −0.75 to +0.6 V (vs. Ag/AgCl) at a scan rate of 10 mV s^{-1}. For all the samples, the illumination was from the backside of the fluorine-doped tin oxide (FTO) glass with an area of 1 cm^2. All the potentials were calibrated to the RHE according to the below equations:

$$\mathrm{E(vs.\ RHE)} = \mathrm{Evs.Ag/AgCl} + 0.197 + 0.059V \times pH \quad (1)$$

Electrochemical impedance spectroscopy (EIS) was carried out by applying an AC voltage amplitude of 10 mV over a frequency range of 10^5–0.01 Hz at an open circuit potential under AM 1.5G illumination.

The applied bias photon-to-current efficiency (ABPE) for water splitting was calculated from the J–V curve according to the following equation:

$$\mathrm{ABPE} = \frac{I\left(mA{\cdot}cm^{-2}\right) \times (1.23 - V_{bias})(V)}{P_{light}(mW{\cdot}cm^{-2})} \times 100\% \quad (2)$$

where I is the photocurrent density at a specific potential, V_{bias} is the applied bias between WE and RHE and P_{light} is the incident illumination power density (100 mW cm^{-2}).

4. Conclusions

An Ni@NiO/$BiVO_4$ three-component heterostructure photoanode was designed and prepared for efficient water splitting through the deposition of Ni particles on the surface of $BiVO_4$ with subsequent thermal treatment. The PEC performance and the working mechanism were investigated, and the results indicate that the formation of the heterostructure can efficiently promote the charge separation. More importantly, the integration of the Ni@NiO structure enables the passivation of the surface states and accelerates the oxygen evolution kinetics on the surface of $BiVO_4$, consequently leading to a significantly enhanced PEC performance. The optimized Ni@NiO/$BiVO_4$ photoanode delivered a photocurrent density of 2.6 mA/cm^2 and a surface charge separation efficiency of nearly 80% at the potential of 1.23 V_{RHE}, which is much better than the bare $BiVO_4$ (1.8 mA/cm^2, 64%). Additionally, the Ni@NiO/$BiVO_4$ photoanode also exhibits good photoelectrochemical stability; the photocurrent density is 2.2 times that of $BiVO_4$ after a 60 min long-term operation.

Supplementary Materials: The following supporting information can be downloaded at: https://www.mdpi.com/article/10.3390/catal12111456/s1, Figure S1: XRD patterns of the different photoanodes; Figure S2: XRD patterns of (a) Ni nanoparticles and (b) the sample after annealing; Figure S3:

TEM images of the different photoanodes; Figure S4: LSV curves of Ni@NiO/$BiVO_4$ films obtained by different conditions; Figure S5: Cyclic voltammograms of the photoanodes measured at scan rates ranging from 20 mV/s to 120 mV/s; Figure S6: OCP values of the different photoanodes; Figure S7: (a) LSV, (b) ABPE and (c) Surface charge separation efficiency of $BiVO_4$ and Ni@NiO/$BiVO_4$ films after PEC tests; (d) Ni 2p XPS spectrum of the Ni@NiO/$BiVO_4$ film after PEC test. References [50–54] are cited in the Supplementary Materials.

Author Contributions: H.L., J.-J.W. and S.-Y.G. conceptualized and supervised the research; S.-S.Z. and J.-Y.C. performed all the experiments and wrote the manuscript revised by J.-J.W.; Y.Z. (Yang Zou), Y.Z. (Yan Zhang), S.-Y.Y. and T.-T.L. participated in various aspects of the experiments and discussions. All authors have read and agreed to the published version of the manuscript.

Funding: This research was funded by National Natural Science Foundation of China, grant number 22279075; Shandong Provincial Natural Science Foundation, grant number [ZR2020YQ09]; QiLu Young Scientist Program of Shandong University; Shenzhen Fundamental Research Program, grant number [JCYJ20190807093411445].

Data Availability Statement: Data supporting reported results of this study are available in the Supplementary Materials of this article and can be obtained from the corresponding author.

Acknowledgments: The authors want to thank Collaborative Innovation Center of Technology and Equipment for Biological Diagnosis and Therapy in Universities of Shandong for their support.

Conflicts of Interest: The authors declare no conflict of interest.

References

1. Gratzel, M. Photoelectrochemical cells. *Nature* **2001**, *414*, 338–344. [CrossRef] [PubMed]
2. Sivula, K.; van de Krol, R. Semiconducting materials for photoelectrochemical energy conversion. *Nat. Rev. Mater.* **2016**, *1*, 1–16. [CrossRef]
3. Xu, X.T.; Pan, L.; Zhang, X.W.; Wang, L.; Zou, J.J. Rational design and construction of cocatalysts for semiconductor-based photo-electrochemical oxygen evolution: A comprehensive review. *Adv Sci.* **2019**, *6*, 1801505. [CrossRef] [PubMed]
4. Zhang, B.; Huang, X.; Zhang, Y.; Lu, G.; Chou, L.; Bi, Y. Unveiling the activity and stability origin of $BiVO_4$ photoanodes with FeNi oxyhydroxides for oxygen evolution. *Angew. Chem. Int. Ed.* **2020**, *59*, 18990–18995. [CrossRef]
5. Cao, X.; Xu, C.; Liang, X.; Ma, J.; Yue, M.; Ding, Y. Rationally designed/assembled hybrid $BiVO_4$-based photoanode for enhanced photoelectrochemical performance. *Appl. Catal. B Environ.* **2020**, *260*, 118136. [CrossRef]
6. Wang, S.C.; He, T.W.; Yun, J.H.; Hu, Y.X.; Xiao, M.; Du, A.J.; Wang, L.Z. New Iron-Cobalt Oxide Catalysts Promoting $BiVO_4$ Films for Photoelectrochemical Water Splitting. *Adv. Funct. Mater.* **2018**, *28*, 1802685. [CrossRef]
7. Pan, J.B.; Wang, B.H.; Wang, J.B.; Ding, H.Z.; Zhou, W.; Liu, X.; Zhang, J.R.; Shen, S.; Guo, J.K.; Chen, L.; et al. Activity and Stability Boosting of an Oxygen-Vacancy-Rich $BiVO_4$ Photoanode by NiFe-MOFs Thin Layer for Water Oxidation. *Angew. Chem. Int. Ed.* **2021**, *60*, 1433–1440. [CrossRef]
8. Zhou, S.Q.; Chen, K.Y.; Huang, J.W.; Wang, L.; Zhang, M.Y.; Bai, B.; Liu, H.; Wang, Q.Z. Preparation of heterometallic CoNi-MOFs-modified $BiVO_4$: A steady photoanode for improved performance in photoelectrochemical water splitting. *Appl. Catal. B Environ.* **2020**, *266*, 118513. [CrossRef]
9. Zachaus, C.; Abdi, F.F.; Peter, L.M.; van de Krol, R. Photocurrent of $BiVO_4$ is limited by surface recombination, not surface catalysis. *Chem. Sci.* **2017**, *8*, 3712–3719. [CrossRef]
10. Wu, M.; Ding, T.; Wang, Y.; Zhao, W.; Xian, H.; Tian, Y.; Zhang, T.; Li, X. Rational construction of plasmon Au assisted ferroelectric-$BaTiO_3$/Au/g-C_3N_4 Z-scheme system for efficient photocatalysis. *Catal. Today* **2020**, *355*, 311–318. [CrossRef]
11. Isimjan, T.T.; Maity, P.; Llorca, J.; Ahmed, T.; Parida, M.R.; Mohammed, O.F.; Idriss, H. Comprehensive Study of All-Solid-State Z-Scheme Photocatalytic Systems of ZnO/Pt/CdZnS. *ACS Omega* **2017**, *2*, 4828–4837. [CrossRef] [PubMed]
12. Wang, C.C.; Chou, P.H.; Yu, Y.H.; Kei, C.C. Deposition of Ni nanoparticles on black TiO_2 nanowire arrays for photoelectrochemical water splitting by atomic layer deposition. *Electrochim. Acta* **2018**, *284*, 211–219. [CrossRef]
13. Ding, C.M.; Shi, J.Y.; Wang, Z.L.; Li, C. Photoelectrocatalytic water splitting: Significance of cocatalysts, electrolyte, and interfaces. *ACS Catal.* **2017**, *7*, 675–688. [CrossRef]
14. Han, T.T.; Shi, Y.Y.; Song, X.X.; Mio, A.; Valenti, L.; Hui, F.; Privitera, S.; Lombardo, S.; Lanza, M. Ageing mechanisms of highly active and stable nickel-coated silicon photoanodes for water splitting. *J. Mater. Chem. A.* **2016**, *4*, 8053–8060. [CrossRef]
15. Lee, S.A.; Lee, T.H.; Kim, C.; Lee, M.G.; Choi, M.-J.; Park, H.; Choi, S.; Oh, J.; Jang, H.W. Tailored NiO_x/Ni cocatalysts on silicon for highly efficient water splitting photoanodes via pulsed electrodeposition. *ACS Catal.* **2018**, *8*, 7261–7269. [CrossRef]
16. Laskowski, F.A.L.; Nellist, M.R.; Venkatkarthick, R.; Boettcher, S.W. Junction behavior of n-Si photoanodes protected by thin Ni elucidated from dual working electrode photoelectrochemistry. *Energy Environ. Sci.* **2017**, *10*, 570–579. [CrossRef]

17. Malara, F.; Fracchia, M.; Kmentová, H.; Psaro, R.; Vertova, A.; Oliveira de Souza, D.; Aquilanti, G.; Olivi, L.; Ghigna, P.; Minguzzi, A.; et al. Direct Observation of Photoinduced Higher Oxidation States at a Semiconductor/Electrocatalyst Junction. *ACS Catal.* **2020**, *10*, 10476–10487. [CrossRef]
18. Kim, T.W.; Choi, K.-S. Nanoporous $BiVO_4$ Photoanodes with Dual-Layer Oxygen Evolution Catalysts for Solar Water Splitting. *Science* **2014**, *343*, 990–994. [CrossRef]
19. Zhang, X.; Zhai, P.; Zhang, Y.; Wu, Y.; Wang, C.; Ran, L.; Gao, J.; Li, Z.; Zhang, B.; Fan, Z.; et al. Engineering single-atomic Ni-N_4-O sites on semiconductor photoanodes for high-performance photoelectrochemical water splitting. *J. Am. Chem. Soc.* **2021**, *143*, 20657–20669. [CrossRef]
20. Zhou, B.X.; Ding, S.S.; Yang, K.X.; Zhang, J.; Huang, G.F.; Pan, A.L.; Hu, W.Y.; Li, K.; Huang, W.Q. Generalized Synthetic Strategy for Amorphous Transition Metal Oxides-Based 2D Heterojunctions with Superb Photocatalytic Hydrogen and Oxygen Evolution. *Adv. Funct. Mater.* **2021**, *31*, 2009230. [CrossRef]
21. Muhmood, T.; Xia, M.Z.; Lei, W.; Wang, F.Y.; Khan, M.A. Design of Graphene Nanoplatelet/Graphitic Carbon Nitride Heterojunctions by Vacuum Tube with Enhanced Photocatalytic and Electrochemical Response. *Eur. J. Inorg. Chem.* **2018**, *2018*, 1726–1732. [CrossRef]
22. Mahmood, A.; Muhmood, T.; Ahmad, F. Carbon nanotubes heterojunction with graphene like carbon nitride for the enhancement of electrochemical and photocatalytic activity. *Mater. Chem. Phys.* **2022**, *278*, 125640. [CrossRef]
23. Muhmood, T.; Xia, M.Z.; Lei, W.; Wang, F.Y. Under vacuum synthesis of type-I heterojunction between red phosphorus and graphene like carbon nitride with enhanced catalytic, electrochemical and charge separation ability for photodegradation of an acute toxicity category-III compound. *Appl. Catal. B Environ.* **2018**, *238*, 568–575. [CrossRef]
24. Ma, Z.; Song, K.; Wang, L.; Gao, F.; Tang, B.; Hou, H.; Yang, W. $WO_3/BiVO_4$ type-II heterojunction arrays decorated with oxygen-deficient ZnO passivation layer: A highly efficient and stable photoanode. *ACS Appl. Mater. Interfaces* **2019**, *11*, 889–897. [CrossRef] [PubMed]
25. Liu, C.; Zhou, J.; Su, J.; Guo, L. Turning the unwanted surface bismuth enrichment to favourable $BiVO_4$/BiOCl heterojunction for enhanced photoelectrochemical performance. *Appl. Catal. B Environ.* **2019**, *241*, 506–513. [CrossRef]
26. Hongmanorom, P.; Ashok, J.; Chirawatkul, P.; Kawi, S. Interfacial synergistic catalysis over Ni nanoparticles encapsulated in mesoporous ceria for CO_2 methanation. *Appl. Catal. B.* **2021**, *297*, 120454. [CrossRef]
27. Malara, F.; Fabbri, F.; Marelli, M.; Naldoni, A. Controlling the surface energetics and kinetics of hematite photoanodes through few atomic layers of NiO_x. *ACS Catal.* **2016**, *6*, 3619–3628. [CrossRef]
28. Jian, J.; Shi, Y.; Ekeroth, S.; Keraudy, J.; Syväjärvi, M.; Yakimova, R.; Helmersson, U.; Sun, J. A nanostructured NiO/cubic SiC p–n heterojunction photoanode for enhanced solar water splitting. *J. Mater. Chem. A.* **2019**, *7*, 4721–4728. [CrossRef]
29. Cai, Q.; Hong, W.; Jian, C.; Liu, W. Ultrafast hot ion-exchange triggered electrocatalyst modification and interface engineering on silicon photoanodes. *Nano Energy* **2020**, *70*, 104485. [CrossRef]
30. Huang, Y.; Jiang, L.-W.; Liu, H.; Wang, J.-J. Electronic structure regulation and polysulfide bonding of Co-doped $(Ni, Fe)_{1+x}S$ enable highly efficient and stable electrocatalytic overall water splitting. *Chem. Eng. J.* **2022**, *441*, 136121. [CrossRef]
31. Chen, H.; Wang, S.C.; Wu, J.Z.; Zhang, X.C.; Zhang, J.; Lyu, M.Q.; Luo, B.; Qian, G.R.; Wang, L.Z. Identifying dual functions of rGO in a $BiVO_4$/rGO/NiFe-layered double hydroxide photoanode for efficient photoelectrochemical water splitting. *J. Mater. Chem. A.* **2020**, *8*, 13231–13240. [CrossRef]
32. Srimurugan, V.; Jothiprakash, C.G.; Souparnika, V.; Prasanth, R. Photocorrosion-less stable heterojunction photoanode for efficient visible-light driven solar hydrogen generation. *Int. J. Hydrogen Energy* **2022**, *47*, 12515–12527. [CrossRef]
33. Ren, S.J.; Sun, M.; Guo, X.T.; Liu, X.H.; Zhang, X.Y.; Wang, L. Interface-confined surface engineering via photoelectrochemical etching toward solar neutral water splitting. *ACS Catal.* **2022**, *12*, 1686–1696. [CrossRef]
34. Zhu, S.S.; Zhang, Y.; Zou, Y.; Guo, S.Y.; Liu, H.; Wang, J.J.; Braun, A. $Cu_2S/BiVO_4$ Heterostructure Photoanode with Extended Wavelength Range for Efficient Water Splitting. *J. Phys. Chem. C.* **2021**, *125*, 15890–15898. [CrossRef]
35. Zhang, Y.; Huang, Y.; Zhu, S.S.; Liu, Y.Y.; Zhang, X.; Wang, J.J.; Braun, A. Covalent S-O Bonding Enables Enhanced Photoelectrochemical Performance of Cu_2S/Fe_2O_3 Heterojunction for Water Splitting. *Small* **2021**, *17*, 2100320. [CrossRef] [PubMed]
36. Zhao, J.H.; Guo, Y.; Cai, L.L.; Li, H.; Wang, K.X.Z.; Cho, I.S.; Lee, C.H.; Fan, S.H.; Zheng, X.L. High-performance ultrathin $BiVO_4$ photoanode on textured polydimethylsiloxane substrates for solar water splitting. *ACS Energy Lett.* **2016**, *1*, 68–75. [CrossRef]
37. Tran-Phu, T.; Fusco, Z.; Di Bernardo, I.; Lipton-Duffin, J.; Toe, C.Y.; Daiyan, R.; Gengenbach, T.; Lin, C.H.; Bo, R.H.; Nguyen, H.T.; et al. Understanding the role of vanadium vacancies in $BiVO_4$ for efficient photoelectrochemical water oxidation. *Chem. Mater.* **2021**, *33*, 3553–3565. [CrossRef]
38. Zhao, L.; Zhang, Y.; Zhao, Z.L.; Zhang, Q.H.; Huang, L.B.; Gu, L.; Lu, G.; Hu, J.S.; Wan, L.J. Steering elementary steps towards efficient alkaline hydrogen evolution via size-dependent Ni/NiO nanoscale heterosurfaces. *Natl. Sci. Rev.* **2020**, *7*, 27–36. [CrossRef]
39. Huang, Y.; Jiang, L.W.; Liu, X.L.; Tan, T.; Liu, H.; Wang, J.J. Precisely engineering the electronic structure of active sites boosts the activity of iron-nickel selenide on nickel foam for highly efficient and stable overall water splitting. *Appl. Catal. B Environ.* **2021**, *299*, 120678. [CrossRef]
40. Jiang, W.J.; Tang, T.; Zhang, Y.; Hu, J.S. Synergistic Modulation of Non-Precious-Metal Electrocatalysts for Advanced Water Splitting. *Acc. Chem. Res.* **2020**, *53*, 1111–1123. [CrossRef]

41. Zhong, M.; Hisatomi, T.; Kuang, Y.; Zhao, J.; Liu, M.; Iwase, A.; Jia, Q.; Nishiyama, H.; Minegishi, T.; Nakabayashi, M.; et al. Surface modification of CoO_x loaded $BiVO_4$ photoanodes with ultrathin p-type NiO layers for improved solar water oxidation. *J. Am. Chem. Soc.* **2015**, *137*, 5053–5060. [CrossRef] [PubMed]
42. Li, F.; Li, J.; Gao, L.L.; Hu, Y.P.; Long, X.F.; Wei, S.Q.; Wang, C.L.; Jin, J.; Ma, J.T. Construction of an efficient hole migration pathway on hematite for efficient photoelectrochemical water oxidation. *J. Mater. Chem. A* **2018**, *6*, 23478–23485. [CrossRef]
43. Yu, F.; Li, F.; Yao, T.; Du, J.; Liang, Y.; Wang, Y.; Han, H.; Sun, L. Fabrication and kinetic study of a ferrihydrite-modified $BiVO_4$ photoanode. *ACS Catal.* **2017**, *7*, 1868–1874. [CrossRef]
44. Gu, S.N.; Li, W.J.; Wang, F.Z.; Wang, S.Y.; Zhou, H.L.; Li, H.D. Synthesis of buckhorn-like $BiVO_4$ with a shell of CeO_x nanodots: Effect of heterojunction structure on the enhancement of photocatalytic activity. *Appl. Catal. B* **2015**, *170*, 186–194. [CrossRef]
45. Zhang, B.; Yu, S.; Dai, Y.; Huang, X.; Chou, L.; Lu, G.; Dong, G.; Bi, Y. Nitrogen-incorporation activates $NiFeO_x$ catalysts for efficiently boosting oxygen evolution activity and stability of $BiVO_4$ photoanodes. *Nat. Commun.* **2021**, *12*, 1–8. [CrossRef] [PubMed]
46. Feng, J.Y.; Huang, H.T.; Guo, W.X.; Xu, X.M.; Yao, Y.F.; Yu, Z.T.; Li, Z.S.; Zou, Z.G. Evaluating the promotional effects of WO_3 underlayers in $BiVO_4$ water splitting photoanodes. *Chem. Eng. J.* **2021**, *417*, 128095. [CrossRef]
47. Huang, G.P.; Fan, R.L.; Zhou, X.X.; Xu, Z.H.; Zhou, W.Y.; Dong, W.; Shen, M.R. A porous Ni-O/Ni/Si photoanode for stable and efficient photoelectrochemical water splitting. *ChemComm* **2019**, *55*, 377–380. [CrossRef]
48. Zhang, Y.; Yuan, S.Y.; Zou, Y.; Li, T.T.; Liu, H.; Wang, J.J. Enhanced charge separation and conductivity of hematite enabled by versatile NiSe2 nanoparticles for improved photoelectrochemical water oxidation. *Appl. Mater. Today* **2022**, *28*, 101552. [CrossRef]
49. Yang, F.; Chen, J.; Ye, Z.; Ding, D.; Myung, N.V.; Yin, Y. Ni-based Plasmonic/Magnetic Nanostructures as Efficient Light Absorbers for Steam Generation. *Adv. Funct. Mater.* **2020**, *31*, 2006294. [CrossRef]
50. Fang, W.Q.; Lin, Y.M.; Xv, R.Z.; Fu, L. Boosting Photoelectrochemical Performance of $BiVO_4$ Photoanode by Synergistic Effect of $WO_3/BiVO_4$ Heterojunction Construction and NiOOH Water Oxidation Modification. *ACS Appl. Energy Mater.* **2022**, *5*, 11402–11412. [CrossRef]
51. Zhang, S.; Lu, Y.; Ding, Q.; Yu, Y.; Huo, P.; Shi, W.; Xu, D. MOF derived NiO thin film formed p-n heterojunction with $BiVO_4$ photoelectrode for enhancement of PEC performance. *Colloids Surf. A* **2022**, *655*, 130282. [CrossRef]
52. Zeng, G.H.; Wang, X.J.; Yu, X.; Guo, J.; Zhu, Y.; Zhang, Y.M. Ultrathin g-C_3N_4/Mo:$BiVO_4$ photoanode for enhanced photoelectrochemical water oxidation. *J. Power Sources* **2019**, *444*, 227300. [CrossRef]
53. Liu, C.H.; Luo, H.; Xu, Y.; Wang, W.C.; Liang, Q.; Mitsuzaki, N.; Chen, Z.D. Cobalt-phosphate-modified Mo:$BiVO_4$ mesoporous photoelectrodes for enhanced photoelectrochemical water splitting. *J. Mater. Sci.* **2019**, *54*, 10670–10683. [CrossRef]
54. Sun, L.X.; Sun, J.H.; Yang, X.J.; Bai, S.L.; Feng, Y.J.; Luo, R.X.; Li, D.Q.; Chen, A.F. An integrating photoanode consisting of $BiVO_4$, rGO and LDH for photoelectrochemical water splitting. *Dalton Trans.* **2019**, *48*, 16091–16098. [CrossRef] [PubMed]